Interfacial phase-change and geometry modify nanoscale pattern formation in irradiated thin films

Tyler P. Evans[1] (ID) · Scott A. Norris[2]

Abstract

In this paper, we consider the linear stability of ion-irradiated thin films where the typical no-penetration boundary condition has been relaxed to a phase-change or mass conservation boundary condition. This results in the modification of the bulk velocity field by the density jump across the amorphous–crystalline interface as new material enters the film and instantaneously changes volume. In other physical systems, phase change at a moving boundary is known to affect linear stability, but such an effect has not yet been considered in the context of continuum models of ion-induced nanopatterning. We also determine simple closed-form expressions for the amorphous–crystalline interface in terms of the free interface, appealing directly to the physics of the collision cascade, which was recently shown to strongly modify the critical angle at which pattern formation is predicted to begin on an irradiated target. We find that phase-change at the amorphous–crystalline boundary imparts a strong ion, target, and energy dependence and, alongside a precise description of the interfacial geometry, may contribute to a unified, predictive, and continuum-type model of ion-induced nanopatterning valid across a wide range of systems. In particular, we consider argon-irradiated silicon, where the presence of phase-change at the amorphous–crystalline interface appears to predict an experimentally observed, strong suppression of pattern formation near 1.5 keV for that system.

Keywords Continuum modeling · Ion-beam sputtering · Pattern formation · Nanopatterning · Thin films

✉ Tyler P. Evans
evans.tyler@utah.edu

1 Department of Mathematics, University of Utah, Salt Lake City, UT 84112, USA

2 Department of Mathematics, Southern Methodist University, Dallas, TX 75275, USA

1 Introduction

Self-organized nanoscale pattern formation has been observed on semiconductor surfaces irradiated by broad ion beams since at least the 1960s [1]. Most commonly, when the ion beam is inclined relative to the surface normal above a critical angle θ_C, black ripples appear with wavevector oriented in the projected downbeam direction of the ion beam, and with wavelengths in the tens or hundreds of nanometers depending on the beam's energy. Sometimes, especially on two-component or metal-seeded targets, irradiation produces highly ordered structures such as hexagonal arrays of nanoscale dots [2]. The potential to understand and exploit these phenomena for high-precision nanoscale engineering at low cost has fueled decades of theoretical and experimental work (see reviews such as [3–6]), especially given significant existing use of ion beams in the semiconductor industry, and an ever-growing array of industrial applications that would benefit from low-cost control over nanometer length scales. However, although the mathematical framework of pattern formation theory [7, 8] provides a powerful tool to understand these phenomena at a general level, the large number of experimental parameters and associated, competing physical mechanisms has frustrated the development of a first-principles model capable of unifying all experimental observations [5].

Soon after the earliest observations of ion-induced self-organization, theoretical approaches focused on modeling the "collision cascade" of atomic displacements that result from an energetic ion impact [9, 10]. Some of these displaced atoms are sputtered away from the target entirely ("erosion"), and it was realized early on that this process could destabilize the surface [10, 11]. Many other atoms remain within the target at new locations ("redistribution"), and in time,it was discovered that these atoms had their own complementary effect on stability [12, 13]. An advantage of this "atomistic" approach is that it exists within a long tradition of parallel inquiry through computer simulation of single impacts, using, for example, full Molecular Dynamics (MD) [14, 15] or the simplified, much faster Binary Collision Approximation (BCA) [16, 17]. This synergy led eventually to the "Crater Function Framework" [18–20]—a "coarse-graining" approach that enables the determination of model terms and coefficients directly from the statistics of single ion impact simulations. However, despite its advantages, this approach only considers the evolution of the free surface, and treats the underlying irradiated film as completely static, likely omitting important physics.

In contrast, several recent developments have suggested the importance of capturing sub-surface dynamics using continuum modeling [21–24], which appear to be capable of significantly influencing pattern formation. In particular, it has been shown that room-temperature bombardment of semiconductors destroys the crystal lattice within a layer near the surface, creating an amorphized film atop the target [25–33], and it has been proposed for some time that this film could be effectively modeled as a Newtonian fluid with an "ion-enhanced" fluidity that, while remaining small compared to typical liquids, is much larger than non-irradiated solids [21]. This fluidity allows the relaxation of surface energy [22] as first analyzed by Orchard [34], as well as of significant internal stresses that build up in the layer [35–41]. Although considered on a phenomenological basis, models based on this "hydrodynamic" approach have led

to striking agreement between theory and experiment within the continuum literature for at least some experimental systems [23, 24, 42–45].

Intriguingly, both the atomistic *and* hydrodynamic perspectives have led to predictions encouragingly similar to experimental observations [19, 24]. This naturally leads to questions on the relative magnitude of what are ultimately two different physical mechanisms, and preliminary studies suggest that a complete model of nanopatterning must eventually contain both [43]. Unfortunately, progress toward a unified theoretical framework bridging the two approaches has been slow, hampered by a large number of physical mechanisms operating simultaneously (e.g., ion collision dynamics [9–11, 46, 47], defect generation and diffusion, stress buildup and relaxation [33, 40, 48, 49], surface energy minimization [34, 50, 51]), and a correspondingly large number of parameters needed to characterize a given experiment (e.g., target species, ion species, ion energy, ion flux, irradiation angle [3–6]). Nevertheless, progress has been made by employing the pattern-forming framework described by Cross, Hohenberg, and Greenside [7, 8] to develop predictions on (a) the presence or absence of spontaneous pattern formation for a given experimental system, (b) the geometric characteristics of patterns when present (e.g., ripple wavelength and orientation), and (c) the critical parameter values (e.g., ion beam energy and incidence angle) at which patterns appear or disappear. Much of our own group's research has focused on the development and study of increasingly comprehensive models of the early stages of pattern formation, when surface amplitudes are small and governing equations can accordingly be linearized, and, in general, we have found that models remain incomplete, requiring additional physics to yield increased predictive power [5].

In this work, we present innovations at the modeling level consisting of (a) an improved model for the location of the lower film boundary, that reproduces experimental data on angle-dependent film thickness more closely than past treatments; and (b) an accounting for the change in density that occurs at this lower boundary due to target amorphization. Our analysis yields three primary findings: (1) the improved modeling of this boundary produces a stark nonlinearity in the dependence of the film stability on the irradiation parameters; (2) many parameters in the resulting model can be estimated directly from software packages that simulate ion–solid interactions; and (3) the resulting predictions are consistent with experimental observations of pattern suppression for certain ion-target combinations when beam energy is increased above a certain value [52, 53]. These findings further develop the insights provided by hydrodynamic models of stress buildup and relaxation, yet also highlight the need for greater experimental effort to understand the behavior of important parameters within this framework.

2 Problem formulation

In this section, we present a continuum model for the ion-irradiated amorphous semiconductor film, containing many of the physical mechanisms described above, and giving special attention to the ways it deviates from a more traditional fluid model. The most important characteristics of this model are depicted schematically in Fig. 1. There, we see ions with energy E bombard a silicon target (with typical thickness
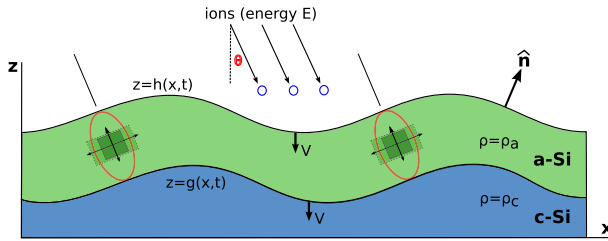
Fig. 1 Schematic depicting the physical system and key aspects of our model. Bombardment of a Silicon wafer by energetic ions leads to amorphization of a thin film of material due to ion-induced collision cascades (red ellipses), sputter erosion of the surface at a velocity V, and the imposition of an anisotropic strain, which can lead to material flow. For ion incidence angles θ above a critical value θ_C, spontaneous formation of ripple patterns is usually observed

in the hundreds of microns) at an incidence angle θ relative to the vertical. Upon arriving at the upper interface $h(x, t)$, the ions penetrate some distance (typically in the nanometer range) before releasing their energy in a roughly elliptical region. The average penetration distance and the size of the ellipse are comparable, and depend on the ion energy. Cumulatively, this process has four primary results. First, it destroys the crystal lattice near the surface, creating a thin amorphous layer of density ρ_a atop a crystalline substrate of density ρ_c, separated by a lower interface $g(x, t)$. Second, the ions impart a strain within the amorphous layer consisting of both isotropic swelling and deviatoric shearing. Third, the ions induce sputter erosion at the upper interface, leading to the gradual recession of the upper interface $z = h(x, t)$ at average speed V. Finally, the recession of the upper interface allows ions to penetrate deeper into the target, causing a corresponding recession of the lower interface $z = g$ at the same average speed V. Our ultimate objective is to understand the evolution of the free surface $h(x, t)$—in particular, to accurately predict the *critical irradiation angle* θ_C at which the surface transitions from flat (stable) to patterned (unstable), as well as the dependence of this critical angle on experimental parameters such as the ion energy. This will in turn require an accurate description of the amorphous film (the crystalline region is assumed to be static).

Conservation laws We begin in typical fashion with the differential form of mass conservation,

$$\frac{\partial \rho}{\partial t} + \nabla \cdot (\rho \vec{v}) = 0, \tag{1}$$

where $\rho = \rho(x, z, t)$ is the density of the amorphous film, and $\vec{v}$ is the velocity field. To accommodate the accumulation of radiation damage over time, we do not assume that the density is constant. Next, we have the differential form of linear momentum conservation,

$$\rho \left(\frac{\partial \vec{v}}{\partial t} + \vec{v} \cdot \nabla \vec{v} \right) = \nabla \cdot \mathbf{T}, \tag{2}$$

where $\mathbf{T}$ is the stress tensor (we ignore body forces such as gravity in this treatment). Because we expect the viscosity of the amorphous film to be very large even despite its radiation-enhanced fluidity (see [50, 51, 53]; see also Chapter 6 of [41]), we take the limit of small Reynolds number, which results in the simplified expression associated with Stokes flow:

$$\nabla \cdot \mathbf{T} = 0. \tag{3}$$

Stress tensor: anisotropic plastic flow We now define the stress tensor $\mathbf{T}$, and in so doing, introduce the first of several irradiation-specific modifications to a typical fluid mechanics model. We let

$$\mathbf{T} = -p\mathbf{I} + 2\eta(\dot{\mathbf{E}} - \dot{\mathbf{E}}_b), \tag{4}$$

where $\dot{\mathbf{E}} = \frac{1}{2}\left(\nabla\vec{v} + \nabla\vec{v}^T\right)$ is the standard linear rate-of-strain tensor, but where the additional term

$$\dot{\mathbf{E}}_b = f A_D \mathbf{D}(\theta) \equiv f A_D \begin{bmatrix} \frac{3}{2}\cos(2\theta) - \frac{1}{2} & 0 & \frac{3}{2}\sin(2\theta) \\ 0 & 1 & 0 \\ \frac{3}{2}\sin(2\theta) & 0 & -\frac{3}{2}\cos(2\theta) - \frac{1}{2} \end{bmatrix} \tag{5}$$

describes a phenomenon known as *Anisotropic Plastic Flow* (APF) [24, 37, 54–57]. Here f is the ion flux (through a plane perpendicular to the beam), A_D is a proportionality constant, and the matrix $\mathbf{D}$ describes a purely deviatoric flattening in the direction $\langle\sin(\theta), 0, -\cos(\theta)\rangle$ of the ion beam, accompanied by expansion in the orthogonal direction. This simultaneous beam-oriented thinning and orthogonal expansion is also sometimes known as "ion hammering" or a "pancake strain."

Equation of state: ion-induced swelling Next, we turn to the equation of state, where we encounter a second irradiation-specific feature of our model. As noted above, we do not assume the film to have a constant density; instead, we propose a simple model of the form

$$\rho(\Delta) = \frac{\rho_a}{1 + \Delta(x, z, t)}, \tag{6}$$

where ρ_a is the initial density of the freshly-amorphized material, and the variable Δ represents radiation-induced "volumization", which obeys a simple advection equation of the form

$$\frac{\partial\Delta}{\partial t} + \vec{v} \cdot \nabla\Delta = f A_I \tag{7}$$

with f again the ion flux, and A_I a proportionality constant. Optionally, Eqs. (6) and (7) can be combined and, with the aid of Eq. (1), replaced by the single equation

$$\nabla \cdot \vec{v} = \frac{\rho}{\rho_a} f A_I. \tag{8}$$

These equations describe the phenomenon of *Ion-Induced Swelling* (IIS) [58–65], in which the accumulation of radiation-induced damage results in a gradual increase in film volume by a (relative) amount $\Delta(x, z, t)$, which accumulates at rate $f A_I$. However, although we forgo a classical incompressibility assumption to allow density to depend on the ion-induced volumization, we continue to omit any dependence on the pressure for mathematical convenience [63]. Hence, this formulation may be thought of as a *quasi-incompressible* approximation.

Top boundary conditions: sputtering At the free upper interface, $z = h(x, t)$, we have

$$v_I = \vec{v} \cdot \hat{\mathbf{n}} - V(\theta)\frac{\rho_c}{\rho},$$
$$[\mathbf{T}] \cdot \hat{\mathbf{n}} = -\gamma \kappa \hat{\mathbf{n}},$$

(9)

where the first equation is the kinematic condition of mass conservation at an interface moving with normal velocity v_I, but *modified* to account for the process of ion-induced sputter erosion at rate $V(\theta)\frac{\rho_c}{\rho}$ at the free surface (see the Appendix of [63] for a derivation). The second is a typical statement of stress balance at a free surface with constant surface energy γ and curvature κ.

Bottom boundary conditions: amorphization At the amorphous–crystalline interface, $z = g(x, t)$, we have

$$\Delta = 0 \quad \longrightarrow \quad \rho = \rho_a$$

(10)

stating that the density immediately on the amorphous side of the amorphous–crystalline boundary should be ρ_a, as newly amorphized material has had no time to be acted upon by IIS. Next, we need boundary conditions on the velocity field. In contrast to prior studies, which have so far all employed the classic "no-penetration" condition, we here use a generalized mass conservation condition on the normal component of the velocity field:

$$[[\rho \vec{v}]] \cdot \hat{\mathbf{n}} = [[\rho]]v_I,$$

(11)

where $[[\cdot]]$ denotes the jump across the interface, and v_I is the normal velocity of the interface itself. This expression accounts for the fact that the amorphous–crystalline boundary is associated with a *phase-change* from crystalline to amorphous, and that the density of the two phases may not be equal [66]. For instance, if the density of the amorphous phase is lower than the density of the crystalline phase, then conservation of mass requires that the velocity on the amorphous side of a moving interface be non-zero. Finally, we need a condition on the tangential velocity, and we choose the "no-slip" condition

$$\vec{v} \cdot \hat{\mathbf{t}} = 0.$$

(12)

We refer the interested reader to [67] for a more general treatment involving a Navier slip condition, which was found to have a negligible effect for realistic estimates of the slip length.

Remarks From the perspective of traditional fluid mechanics models, the ion irradiation system we study here has five major, unusual features. First, we deduct from the Newtonian viscous stress tensor an ion-induced *stress-free strain rate*, describing a phenomenon often called "ion hammering" [37, 68–70] or "pancake strain" [5, 41]. The resulting angle-dependent shear flow has been shown to be destabilizing for certain irradiation geometries [24]. Second, a modified equation of state [63] is introduced to allow "volumization" due to irradiation damage; however, the model remains "quasi-incompressible" in the sense that the density remains independent on the pressure. Third, the kinematic condition at the top free boundary must be modified to account for target sputtering—i.e., non-conservation of mass—at this surface. Fourth, because amorphization of target material at the bottom boundary induces an instantaneous increase in volume, conservation of mass requires a non-zero normal velocity. Fifth, because the location of the lower interface arises due to amorphization of material in a region anchored to the upper interface, the two interfaces move in tandem. We now turn to a detailed exploration of this relationship, which constitutes one of the major contribution of this work.

3 Lower interface position

Although the model described above is formulated with general upper- and lower-boundary locations $z = h(x, t)$ and $z = g(x, t)$, a final unusual feature of ion-irradiated films, in contrast with more typical fluid systems, is that the locations of these two interfaces are not independent. Rather, they are linked by the irradiation process itself, in which ions induce amorphization over some domain relative to their entry point through the free surface, and this domain *moves deeper into the film* as the surface recedes due to erosion. Hence, variations in the height of the top, free interface $h(x, t)$ should induce corresponding variations in the height of the bottom, amorphous–crystalline interface $g(x, t)$. This correspondence is observable under cross-section TEM imaging [42, 71]). In this section, we review how this relationship has been modeled in the past and propose a meaningful improvement.

Motivation The first work to explicitly include this dependence appears to be [24, 72], which placed the lower interface directly below the upper interface; i.e., a vertical translation,

$$g(x, t) = h(x, t) - h_0. \tag{13}$$

This relationship captures the general correspondence between upper and lower boundaries, and its initial application led to a predicted critical angle $\theta_C = 45°$, in good agreement with experiments [24]. However, it does not exhibit any dependence on the ion incidence angle θ, and in particular fails to describe the thinning of the amorphous film that occurs as the ion beam approaches grazing incidence ($\theta \to 90°$).
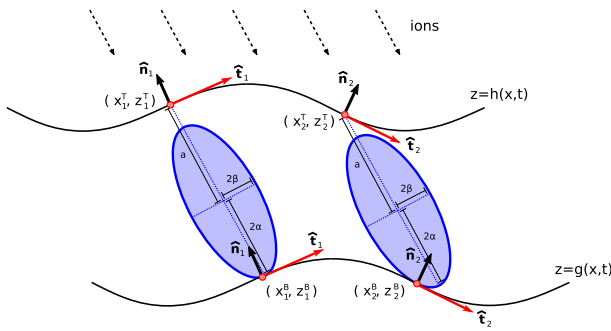
Fig. 2 Schematic depicting Sigmund's approximation of deposited energy using Gaussian ellipses, and illustrating the method of locating the amorphous–crystalline interface that is implied by this approximation

More recently, several authors have proposed an alternative approach [42, 63, 64, 73], in which the lower interface remains a simple translation of the top interface by a distance h_0, but the translation occurs in the direction θ of the incident ion beam, hence

$$g(x, t) = h(x - h_0 \sin(\theta), t) - h_0 \cos(\theta). \tag{14}$$

This highly plausible relationship does exhibit dependence on θ, and, indeed, corresponds to a film that thins as $\theta \rightarrow 90°$. However, whereas Eq. (14) predicts that the film thickness goes to zero at grazing incidence, experiments show that the film retains a comfortably non-zero thickness in this limit [21, 42, 43, 71, 74]. Even more worryingly, when this interface location is used, the predicted bifurcation angle drops from 45° to only 30°, far below the observed value [65].

These concerns motivate a more careful treatment than the simple geometric approaches described above, in hopes of obtaining a result somewhere between Eqs. (13) and (14). We here propose the following strategy:

1 characterizing the region $\Omega_A(\vec{x}_I, \theta)$ amorphized by ions entering at $\vec{x}_I$ at angle θ;
2 constructing a union of amorphous regions Ω_A for all entry points $\vec{x}_I$ on the surface;
3 and identifying the bottom boundary of the region so constructed.

An alternative way of describing this approach is to imagine "dragging" the region $\Omega_A(\vec{x}_I, \theta)$ over the free surface $z = h(x, t)$, in which case, for every point $\langle x_T, z_T \rangle$ on the top surface, there exists a unique corresponding point $\langle x_B, z_B \rangle$ on the bottom surface *with the same slope*, whose location must be determined.

Formulation We begin by characterizing the amorphized region Ω_A, and we follow the well-established model of Sigmund [9, 10], who approximated the average distribution of energy deposited by the collision cascade as a Gaussian ellipsoid oriented along the ion beam (see Fig. 2). Assuming an ion entry point at the origin, and mean, downbeam ion penetration distance a, and standard deviations α and β of energy release in the downbeam and crossbeam directions, the energy distribution for a single ion implantation event is then

$$E_D(\tilde{x}, \tilde{z}) = \frac{1}{2\pi\alpha\beta} \exp\left(-\frac{(\tilde{z}-a)^2}{2\alpha^2} - \frac{\tilde{x}^2}{2\beta^2}\right), \tag{15}$$

where $(\tilde{x}, \tilde{z})$ are co-ordinates oriented in the "crossbeam" and "downbeam" directions, respectively, which can be converted to lab-frame co-ordinates via the transformation

$$\begin{aligned} \tilde{x} &\rightarrow x\cos(\theta) + z\sin(\theta), \\ \tilde{z} &\rightarrow x\sin(\theta) - z\cos(\theta). \end{aligned} \tag{16}$$

We then have, in laboratory (i.e., Cartesian) co-ordinates (x,z),

$$E_D(x, z) = \frac{1}{2\pi\alpha\beta} \exp\left(-\frac{(x\sin(\theta) - z\cos(\theta) - a)^2}{2\alpha^2} - \frac{(x\cos(\theta) + z\sin(\theta))^2}{2\beta^2}\right), \tag{17}$$

Now we consider the level curves of this function. If we introduce the constant $E_0 = \frac{1}{2\pi\alpha\beta}$, and define another constant E_A representing an amorphization threshold, then the ellipse within which amorphization occurs is defined via the expression

$$\begin{aligned} F(x, z) &= \frac{1}{2}\left(\frac{(a + z\cos(\theta) - x\sin(\theta))^2}{\alpha^2} + \frac{(x\cos(\theta) + z\sin(\theta))^2}{\beta^2}\right) \\ &= \ln\left(\frac{E_0}{E_A}\right) = 2, \end{aligned} \tag{18}$$

where we have set $\ln\left(\frac{E_0}{E_A}\right) = 2$ to indicate that we expect amorphization within the second standard deviation boundary. Finally, to find the point on the bottom interface, we invoke the "dragging" analogy, and look for the location on the bottom half of this level curve which has the same slope as the corresponding point on the top curve. This can be stated

$$\nabla F \cdot \langle 1, h_x \rangle = 0, \tag{19}$$

where h_x denotes the slope of the free interface at the point where the ion enters the film. Equations (18) and (19) represent a system of two equations for two unknowns.

A simplifying limit For any ion entry point (x^T, z^T) on the top surface, let us label the corresponding point on the bottom surface (x^B, z^B) as depicted in Fig. 2, and let us furthermore characterize the horizontal and vertical distances between these points using functions $X(\theta, h_x)$ and $Z(\theta, h_x)$ as follows:

$$\begin{aligned} x^B &= x^T + X(\theta, h_x) = x^T + \left[X(\theta, 0) + \frac{\partial X}{\partial h_x}(\theta, 0)h_x + \mathcal{O}\left(h_x^2\right)\right], \\ z^B &= z^T - Z(\theta, h_x) = z^T - \left[Z(\theta, 0) + \frac{\partial Z}{\partial h_x}(\theta, 0)h_x + \mathcal{O}\left(h_x^2\right)\right], \end{aligned} \tag{20}$$

where we have expanded X and Z in the small slope h_x, which is evaluated at $x = x^T$, and where the quantity $\frac{\partial Z}{\partial h_x}(\theta, 0) = 0$ due to the geometry of the construction. Now, because our upper and lower surfaces satisfy $z = h(x, t)$ and $z = g(x, t)$, respectively, it follows from Eqs. (20) that

$$
\begin{aligned}
g\left(x^B, t\right) &= h\left(x^T, t\right) - Z(\theta, 0) + \mathcal{O}\left(h_x^2\right) \\
&= h\left(x^B - X(\theta, 0) - \frac{\partial X}{\partial h_x}(\theta, 0)h_x + \mathcal{O}\left(h_x^2\right), t\right) - Z(\theta, 0) + \mathcal{O}\left(h_x^2\right)
\end{aligned}
\tag{21}
$$

and from here, expanding the expression on the second line in $|h_x| \ll 1$ and keeping only leading order terms gives

$$
g\left(x^B, t\right) = h\left(x^B - X(\theta, 0), t\right) - Z(\theta, 0) + \mathcal{O}\left(h_x^2\right).
\tag{22}
$$

We refer the reader to the Appendix for additional details.

    Result Equation (22) indicates that to leading order in a small slope, the location of the bottom boundary *does not depend on that slope*, and can be found by replacing the tangent vector $\hat{\mathbf{t}} = \langle 1, h_x \rangle$ with the coordinate vector $\hat{\mathbf{i}} = \langle 1, 0 \rangle$ in Eq. (19). Equipped with this knowledge, the solution for the displacement becomes straightforward. The linear equation (19) yields an expression for X in terms of Z which can be substituted into the quadratic equation (18), for which the larger (i.e., more positive) solution is chosen. The result is

$$
\begin{aligned}
x_0(\theta) &= X(\theta, 0) = a\sin(\theta) + 2\left(\frac{(\alpha^2 - \beta^2)\sin(\theta)\cos(\theta)}{\sqrt{\alpha^2\cos^2(\theta) + \beta^2\sin^2(\theta)}}\right), \\
h_0(\theta) &= Z(\theta, 0) = a\cos(\theta) + 2\left(\sqrt{\alpha^2\cos^2(\theta) + \beta^2\sin^2(\theta)}\right),
\end{aligned}
\tag{23}
$$

which are surprisingly concise forms, and all parameters a, α, β may be obtained directly from simulation software, such as SRIM [16]. In principle, we only require that a, α, β describe a bivariate Gaussian that is associated with "damage" to the substrate; we do not strictly require that it be the recoil distribution, power deposition, or any other quantity. In the present work, we use the distribution of the final resting places of the bombarding ions as a proxy for the "damaged region", reasoning that an ion only stops moving once it has deposited all of its energy. Equations (22) and (23) also indicate the strongly appealing feature that the lower interface *remains* a direct translation of the upper interface, but in a more complex direction $\langle x_0(\theta), h_0(\theta) \rangle$ than either the "vertical" case (13) or "diagonal" case (14). In fact, we can define an "effective interface displacement angle"

$$
\Psi(\theta) = \tan^{-1}\left(\frac{x_0(\theta)}{h_0(\theta)}\right)
\tag{24}
$$

that lies in between 0 and θ to characterize this direction.

Some interesting limits We note that the above expressions are easily specialized to previously studied interface relations by taking appropriate limits. First, a certain "angle-independence" limit

$$\lim_{\theta \to 0} x_0(\theta) = 0,$$
$$\lim_{\theta \to 0} h_0(\theta) = (a + 2\alpha) \tag{25}$$

yields the "vertical translation" case used in [24, 72]. Next, the "vanishing cross-beam width" limit

$$\lim_{\beta \to 0} x_0(\theta) = (a + 2\alpha) \sin(\theta),$$
$$\lim_{\beta \to 0} h_0(\theta) = (a + 2\alpha) \cos(\theta) \tag{26}$$

yields the "diagonal translation" relation used in [42, 63, 64]. Finally, the "spherical collisions" limit

$$\lim_{\beta \to \alpha} x_0(\theta) = a \sin(\theta),$$
$$\lim_{\beta \to \alpha} h_0(\theta) = a \cos(\theta) + 2\alpha \tag{27}$$

though receiving less attention recently has been previously considered at least by [12, 75] as a simplifying assumption broadly appropriate for low-energy noble gas ion irradiation of Si.

Comparison to data In Fig. 3, we compare our ellipse-based displacements (23), along with "vertical" and "diagonal" displacements (25)–(26), to angle-dependent data on film thickness inferred from experiments for 1000 eV $Ar^+ \to$ Si [43]. To determine the parameter values a, α, β in Eq. (23), we used the mean and standard deviations of final ion locations as simulated by the Binary Collision Approximation code TRI3DST [17]. It is immediately evident that the predictions by the ellipse-based model, which lie between the "vertical" and "diagonal" models, are much better than either.

4 Linear stability analysis

We have now defined all aspects of our model, and are ready to analyze the predicted stability of the irradiated film to perturbations. In this section, we provide a concise summary of our analysis and a statement of the stability result. Full details of the analysis are described in the Appendix.

Conversion to moving frame Ion bombardment and the associated sputter removal of atoms cause the surface of the target to gradually recede at an average speed V

Fig. 3 Film thickness prediction using theoretical expression $h_0(\theta)$ from Eq. (23) compared to film thickness inferred from [43] for 1keV Ar$^+$ → Si. Model parameters $a = 3.45$, $\alpha = 1.55$, $\beta = 1.38$ were obtained from the final resting positions of ions using simulation software TRI3DST ("BCA"). Also shown are the predictions of the "vertical" translation assumption (25) and the "diagonal" translation assumption (26)
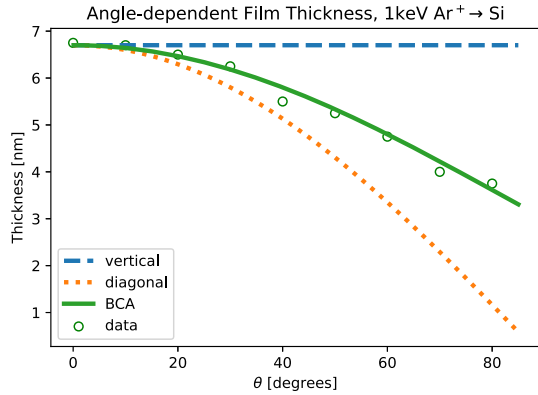
that depends on the ion and target species, the ion energy E and flux f, and the ion incidence angle θ. This speed may be expressed

$$V = f\Omega Y(\theta), \tag{28}$$

where f is the ion flux, Ω is the atomic volume of the target species, and $Y(\theta)$ is the *sputter yield*, which has units of sputtered atoms per incident ion. As described above, the receding free interface $z = h(x, t)$ causes an associated recession of the amorphous–crystalline interface $z = g(x, t)$, and it is convenient to perform analyses in a frame of reference that recedes along with these interfaces. This is accomplished via the substitutions

$$\begin{aligned}
h &\to h - Vt \\
g &\to g - Vt \\
v_{I,h} &\to v_{I,h} - V(\hat{k} \cdot \hat{n}) \\
z &\to z - Vt \\
\vec{v} &\to \vec{v} - V\hat{k},
\end{aligned} \tag{29}$$

The most notable consequence of this conversion is that at the amorphous–crystalline interface $z = g(x, t)$, the velocity in the bulk acquires an additional term $V\hat{k}$—that is, in the moving frame of reference, material now appears to move *through* the bottom boundary with velocity $V\hat{k}$.

   Steady state solution We next look for steady state solutions ($\partial/\partial t \to 0$) consisting of flat surfaces ($g(x, t) = 0$, $h(x, t) = h_0(\theta)$) exhibiting translation symmetry ($\partial/\partial x \to 0$). These assumptions lead to a system of boundary value problems in the variable z.

In the amorphous bulk, we have

$$\frac{\partial}{\partial z}(\rho_0 w_0) = 0,$$
$$\eta u_{0zz} = 0,$$
$$-p_{0z} + 2\eta w_{0zz} = 0, \tag{30}$$
$$\rho_0 = \frac{\rho_a}{1 + \Delta_0},$$
$$w_0 \Delta_{0z} = f A_I.$$

At flat amorphous–crystalline interface $z = 0$, we have

$$\Delta_0 = 0,$$
$$u_0 = 0, \tag{31}$$
$$w_0 = V\left(\frac{\rho_c}{\rho_a}\right),$$

which represent the steady-state equations of the no-slip and mass conservation conditions, respectively, in the downward-translating frame. At the flat-free interface $z = h_0(\theta)$, we have

$$0 = w_0 - V\frac{\rho_c}{\rho_0},$$
$$u_{0,z} = 2f A_D D_{13}, \tag{32}$$
$$p_0 = 2\eta(w_{0z} - f A_D D_{33})$$

as in [65], where the first equation is the steady-state equation of the modified kinematic condition, and the second two equations are due to the steady-state stress balance $\mathbf{T}_0 \cdot \hat{n}_0 = 0$ at the upper interface.

These equations admit solutions $\vec{\Phi}_0(z) = [\rho_0(z), u_0(z), w_0(z), p_0(z), \Delta_0(z)]$ of the form

$$\rho_0(z) = \frac{\rho_a}{\sqrt{1 + 2f A_I \frac{\rho_a}{\rho_c}\frac{z}{V}}},$$
$$u_0(z) = 2f A_D D_{13} z,$$
$$w_0(z) = V\left(\frac{\rho_c}{\rho_a}\right)\sqrt{1 + 2f A_I \frac{\rho_a}{\rho_c}\frac{z}{V}}, \tag{33}$$
$$p_0(z) = \frac{2f A_I \eta}{\sqrt{1 + 2f A_I \frac{\rho_a}{\rho_c}\frac{z}{V}}} - 2f A_D \eta D_{33},$$
$$\Delta_0(z) = \sqrt{1 + 2f A_I \frac{\rho_a}{\rho_c}\frac{z}{V}} - 1,$$

where D_{ij} simply denotes the component of the tensor described in Eq. (5). We note that (a) Anisotropic Plastic Flow causes a linear shear flow in the x direction, (b) Ion-Induced Swelling induces a nontrivial z-dependence in most quantities, and (c) Boundary Amorphization multiplies all instances of the velocity V by $\frac{\rho_c}{\rho_a} > 1$. In the "small swelling" limit discussed below and in our previous work [63–65], we find that this steady state also has an associated steady in-plane stress of

$$\mathbf{T}_{0,xx} = 6 f A_D \eta \cos(2\theta) + 2 f A_I \eta, \tag{34}$$

which we refer to later. See also discussion in [65] where the above expression was compared with experimental results due to [41].

Linearization in normal modes We now expand the governing equations described above in the neighborhood of steady-state solutions, via the expressions

$$\begin{aligned}
\vec{\Phi}(x, z, t) &\to \vec{\Phi}_0(z) + \epsilon \vec{\Phi}_1(x, z, t) \\
h(x, t) &\to h_0(\theta) + \epsilon h_1(x, t) \\
g(x, t) &\to 0 + \epsilon g_1(x, t),
\end{aligned} \tag{35}$$

representing small perturbations $\vec{\Phi}_1 = [\rho_1, u_1, w_1, p_1, \Delta_1]$ to the steady state fields $\vec{\Phi}_0(z)$. The linearized equations occurring at $\mathcal{O}(\epsilon)$ are

$$\begin{aligned}
\rho_{1t} + \rho_0 u_{1x} + \rho_{0z} w_1 + \rho_0 w_{1z} + \rho_{1z} w_0 + \rho_1 w_{0z} &= 0, \\
-p_{1x} + \eta(2 u_{1xx} + u_{1zz} + w_{1xz}) &= 0, \\
-p_{1z} + \eta(w_{1xx} + 2 w_{1zz} + u_{1xz}) &= 0, \\
\rho_1 &= \frac{-\rho^* \Delta_1}{(1 + \Delta_0)^2}, \\
\Delta_{1t} + u_0 \Delta_{1x} + w_0 \Delta_{1z} + w_1 \Delta_{0z} &= 0
\end{aligned} \tag{36}$$

in the amorphous bulk. At amorphous–crystalline interface, $z = 0$,

$$\begin{aligned}
\Delta_{0,z}(z; 0, h_0) g_1 + \Delta_1(z; 0, h_0) &= 0, \\
u_{0z} g_1 + u_1 + g_{1x}(w_0 - V) &= 0, \\
-g_{1x} u_0 + w_{0z} g_1 + w_1 &= \left(\frac{\rho_a - \rho_c}{\rho_a} \right) g_{1t},
\end{aligned} \tag{37}$$

and we note that the last of these is due to conservation of mass at the interface, representing one of the main contributions of the present work. At $z = h_0$,

$$\begin{aligned}
h_{1t} &= w_1 - u_0 h_{1x} + h_1 w_{0z} + \frac{V \rho_c}{\rho_0^2} (\rho_{0z} h_1 + \rho_1,) \\
\eta(u_{1z} + w_{1x}) - h_{1x} T_0^{11} &= 0, \\
-p_1 + 2\eta w_{1z} + T_{0z}^{33} &= 0,
\end{aligned} \tag{38}$$

where the first equation is due to the linearization of the kinematic condition modified to reflect sputtering. For details of its derivation, we refer the reader to [63]. The second two equations are due to the linearization of the stress balance at the free interface,

$$\mathbf{T}_0 \cdot \hat{n}_1 + \left[\frac{\partial \mathbf{T}_0}{\partial z} \cdot h_1 + \mathbf{T}_1 \right] \cdot \hat{n}_0 = \vec{0}, \tag{39}$$

where $\hat{n}_0 = <0, 0, 1>$ and $\hat{n}_1 = <-h_{1x}, -h_{1y}, 0>$. As in [65], T_0^{11} denotes the upper-left component of steady-state stress tensor $\mathbf{T}_0$, and T_0^{33} denotes the bottom-right component. The component indices are denoted as superscripts to distinguish them from the subscripts which elsewhere denote terms in the expansion. We seek solutions to the above linear equations using the ansatz

$$\begin{aligned}
h_1(x,t) &\to \tilde{h}_1 \exp(\sigma t + ikx), \\
g_1(x,t) &\to \tilde{g}_1 \exp(\sigma t + ikx), \\
\vec{\tilde{\Phi}}_1(x,z,t) &\to \vec{\tilde{\Phi}}_1(z) \exp(\sigma t + ikx),
\end{aligned} \tag{40}$$

i.e., we exploit linear superposition to study a single Fourier mode with wavenumber k and look for a solution exhibiting exponential growth or decay at the rate σ. This step leads to a system of boundary value problems for $\vec{\tilde{\Phi}}_1(z)$ that include the growth rate σ as an eigenvalue, implicitly defining $\sigma = \sigma(k)$.

Simplifying limits The boundary value problems resulting from (36)–(38) and the application of the ansatz (40) do not admit a simple closed-form solution. For analytical tractability, we employ two simplifying limits that we have described more fully elsewhere [65]:

- small dimensionless deformation rates $\frac{f A_I h_0(\theta)}{V(\theta)} \ll 1$, $\frac{f A_D h_0(\theta)}{V(\theta)} \ll 1$
- small dimensionless wavenumber $k h_0(\theta) \ll 1$

The first limit is justified by the observation in Ref. [64] that the contribution to the dispersion relation for arbitrary swelling rate A_I—obtained computationally—very closely resembles a constant multiple of the contribution in the small swelling limit $A_I \to 0$, as well as the evident smallness of the parameter as observed experimentally [60–62]. An additional advantage is that these "slow deformation" limits allow the elimination of interaction terms as shown in [65], ensuring linearity in A_I and A_D.

The second limit is justified by the observation that in ion irradiation of pure materials, the transition from stability to instability occurs first at long wavelengths with wavenumbers near $k = 0$ (i.e., the bifurcation is of "Type II" in the classification of Cross and Hohenberg [7, 8]). This wavelength is small compared to the amorphous film thickness, hence we have dimensionless quantity $k h_0(\theta) \ll 1$ available for long-wave expansion.

Exploiting the long-wave limit, we formally expand (in dimensional quantities) as

$$\begin{aligned}
\vec{\tilde{\Phi}}_1(z) &= \vec{\tilde{\Phi}}_{10}(z) + \vec{\tilde{\Phi}}_{11}(z)k + \vec{\tilde{\Phi}}_{12}(z)k^2..., \\
\sigma &= \sigma_0 + \sigma_1 k + \sigma_2 k^2...
\end{aligned} \tag{41}$$

in order to avoid a change of variables, while noting that it is entirely equivalent to the expansion in dimensionless (kh_0). We refer the reader to the Appendix of [65] where a similar retroactive non-dimensionalization was carried out. The expansion above then leads to Eqs. (A.2)–(A.23) in the Appendix of the present work, and their solution provides our main analytical result, Eq. (42).

Dispersion relation With the simplifications just described, the linearized governing equations become tractable, and admit a solution $\vec{\Phi}_1$ with eigenvalue $\sigma(k)$.

Of primary interest to us is the real part of σ:

$$
\begin{aligned}
\mathrm{Re}\,(\sigma) = - \, f\Bigg[& 3A_D \left(\frac{\rho_a}{\rho_c}\right) \frac{\cos\,(2\theta + \Psi(\theta))}{\cos\,(\Psi(\theta))} \\
& + \frac{A_I}{2}\left(\frac{\rho_a}{\rho_c}\right)^2 + \frac{\Omega Y(\theta)}{h_0(\theta)}\left(1 - \frac{\rho_a}{\rho_c}\right)\Bigg](kh_0(\theta))^2 + \dots
\end{aligned}
\tag{42}
$$

where

$$
\tan\,(\Psi(\theta)) = \frac{x_0(\theta)}{h_0(\theta)}
\tag{43}
$$

is again the "effective interface displacement angle" $\Psi(\theta)$ defined in Eq. (24).

Equation (42) reveals the expected pattern-forming behavior of the irradiated surface. If the term in brackets is positive, then long-wave Fourier modes decay, and patterns are suppressed. However, if the term in brackets is negative, then long-wave Fourier modes grow, and patterns are expected to appear. Furthermore, because the term in brackets depends on the incidence angle θ, we can identify the critical angle θ_C at which the system transitions from stability (perturbations decay; no patterns form) to instability (perturbations grow; patterns form).

Discussion Equation (44) is a generalization of previous results [24, 63–65], and can be interpreted accordingly. The first term in Eqs. (44) describes the effect of Anisotropic Plastic Flow (APF), modified here by the effect of differing phase densities and a generalized bottom boundary location. In the limit of equal densities $\rho_a = \rho_c$ and vertical boundary displacement $x_0 = 0$, we recover the long-wavelength limit of the result obtained in Ref. [24]. Similarly, the second term describes the effect of Ion-induced Isotropic Swelling (IIS), again modified by the effect of differing phase densities. In the limit of equal densities we recover the long-wave version of the result obtained in Ref. [63]. The third term, which is new, describes an additional, direct effect of the density change across the lower interface. Like the IIS term, this term is stabilizing for all incidence angles, but unlike that term, its value increases with increasing angle.

We pause to note how Eq. (42) cleanly illustrates the influence of the bottom boundary location by way of the "effective interface displacement angle" $\Psi(\theta)$ appearing in the APF term. At one extreme is the "vertical displacement" approximation $\Psi(\theta) = 0$; this leads to a term of the form $\cos(2\theta)$ in Eq. (42), which changes sign (and hence stability) at 45° as seen in Ref. [24]. At the other extreme is the "diagonal displace-

ment" approximation $\Psi(\theta) = \theta$; this leads to a term of the form $\frac{\cos(3\theta)}{\cos(\theta)}$ in Eqn. (42), which changes sign (and therefore stability) at 30°, as seen in Ref. [65].

For the "ellipsedragging" boundary location proposed here, we expect the APF term to change sign at a intermediate values of θ between 30° and 45°, depending on the shape of the ellipse. Furthermore, even in the absence of IIS, the new stabilizing term associated with boundary amorphization increases the critical angle θ_C somewhat above the value at which the APF term changes sign. Together, and in marked contrast to the "diagonal" translation model, these features provide a means to maintain agreement with experimental observations of $\theta_C \approx 45°$ for the $Ar^+ \rightarrow Si$ system.

5 Results

In this section, we explore the implications of the result (42), including comparison with relevant experimental data, and using the TRI3DST software to estimate relevant collision parameters.

Stability boundary The growth rate in Eq. (42) can be expressed more succinctly if we divide through by $f A_D \frac{\rho_a}{\rho_c}$, yielding the non-dimensional form

$$\text{Re}(\Sigma) = \left[-3\frac{\cos(2\theta + \Psi(\theta))}{\cos(\Psi(\theta))} - \frac{1}{2}P_1 - P_2 R(\theta) \right] (kh_0)^2, \qquad (44)$$

where

$$\begin{aligned}
\Sigma &= \frac{\sigma}{f A_D} \frac{\rho_c}{\rho_a}, \\
P_1 &= \frac{A_I}{A_D} \frac{\rho_a}{\rho_c}, \\
P_2 &= \frac{\Omega Y(0)}{A_D h_0(0)} \left(\frac{\rho_c}{\rho_a} - 1 \right), \\
R(\theta) &= \frac{Y(\theta)}{h_0(\theta)} \frac{h_0(0)}{Y(0)}
\end{aligned} \qquad (45)$$

are all dimensionless. In this formulation, we have separated the third term in brackets into a constant P_2 times an angle-dependent function $R(\theta)$. To determine the critical angle θ_C separating stable parameter combinations ($\Sigma < 0$ for all k) and unstable combinations ($\Sigma > 0$ for some k), we set the coefficient in brackets equal to zero and plot the resulting level curves. This requires a functional form for $R(\theta)$, which contains the yield $Y(\theta)$ and film thickness $h_0(\theta)$. Because our predicted film thickness (20) uses Sigmund's Gaussian ellipse model [10], we also use that model's predictions for sputter yield. The resulting stability phase diagram is shown in Fig. 4, with curves depicting boundaries in (P_2, θ)-space for different values of the parameter P_1.

Comparison to experiment We observe that the stability boundary in Fig. 4 is highly nonlinear, with a sudden increase in the critical angle θ_c from around 50° to 75° in
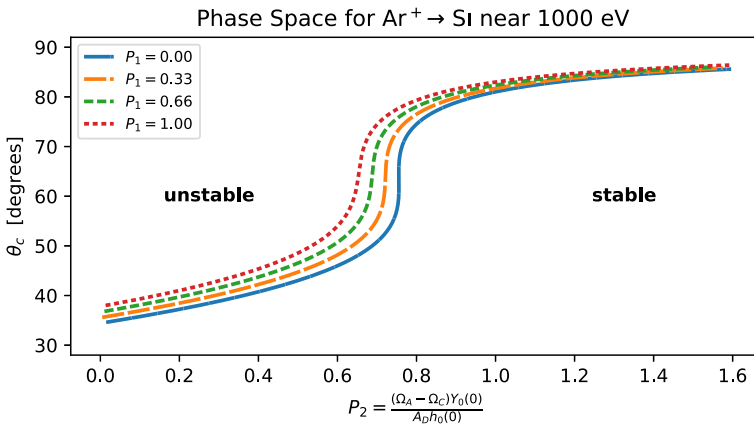
Fig. 4 The critical angle θ_C as a function of the dimensionless phase-change parameter P_2, for various choices of the dimensionless swelling parameter P_1

the vicinity of $P_2 \approx 0.75$. This striking behavior may offer insight into some puzzling behavior of the commonly studied $Ar^+ \rightarrow Si$ system [53]. At an energy of 1 keV, this system exhibits a critical angle $\theta_c \approx 45°$ [76], whereas at higher energies it has been reported that ripples are no longer seen for any incidence angle below 65° [53]. At the time, this lack of patterning could not be explained by any existing models, leading authors to hypothesize the existence of some missing, "unconditionally stabilizing" mechanism [53, 63–65].

As noted above, the new boundary amorphization term $P_2 R(\theta)$ in Eq. (44) is stabilizing for all angles of incidence. Moreover, according to Fig. 4, the 45-degree critical angle observed at 1 keV would imply a value of $P_2 \approx 0.6$, which is rather near the sharp transition from low to high angles of incidence. Hence, if P_2 were to increase even modestly as the energy increases beyond 1 keV, the critical angle would be expected to increase sharply, and could readily surpass the value of 65°, which was the most oblique incidence angle studied in [53].

To explore this possibility further, we attempt to construct energy-dependent estimates for each parameter in the model, and present the associated critical angle predictions. Values of the collision parameters Y, a, α, β are obtained using the simulation package TRI3DST [17], which allows $\Psi(E, \theta)$ and $R(E, \theta)$ to be determined empirically. Based on the findings of [65] that Ion-Induced Swelling does not seem to play a strong role in the $Ar^+ \rightarrow Si$ system, we assume that $A_I \ll A_D$ and so set $P_1 = 0$. Finally, we need an estimate for $P_2(E)$. Within this parameter, the film thickness h_0 and yield Y can readily be determined using TRI3DST, but the Anisotropic Plastic Flow parameter A_D cannot.

The value of A_D is much more difficult to estimate, and existing estimates in the nuclear stopping regime vary quite a bit [39, 43, 77] (although estimates in the electronic stopping regime are fairly well-developed [37, 78]). Here, we take an indirect approach. As noted above in Eq. (34), our model predicts a steady stress of $\mathbf{T}_{0,xx} = 6 f A_D \eta \cos(2\theta)$ when $A_I = 0$, implying that
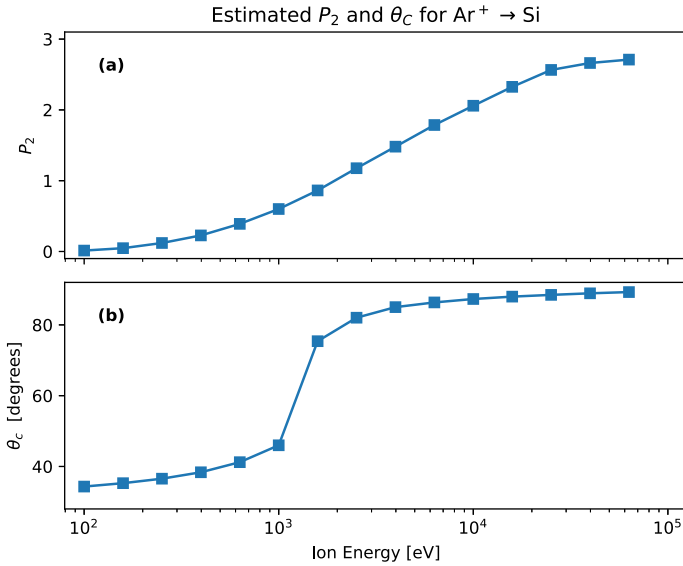
Fig. 5 a Predicted values of the dimensionless parameter P_2 for various energies using the assumptions described in the main text. **b** Associated predicted critical angles obtained from Eq. (44). For the value $P_2^{1\text{keV}} = 0.6$ implied by experimental observations at 1 keV [76], the sharp increase in critical angle occurring around 1.5 keV is consistent with experimental observations at higher energies [53]

$$A_D \sim \eta^{-1} \mathbf{T}_{0,xx}, \tag{46}$$

i.e., a scaling for A_D can be determined from those of fluidity and the steady stress. Now, the work of Davis on ion-assisted deposition [79] has been used to argue that $\mathbf{T}_{0,xx} \sim E^{-\frac{7}{6}}$ for the case of pure ion irradiation without concurrent deposition [42]. Moreover, the work of Vauth and Mayr on ion-enhanced fluidity [50] has frequently been used to argue that $\eta^{-1} \sim \frac{E}{h_0}$ [19, 53, 73, 76, 80]. If we combine these predictions, we obtain

$$P_2(E) \approx P_2^{1\text{keV}} \frac{Y(0, E)}{Y(0, 1\text{keV})} \left(\frac{E}{1\text{keV}} \right)^{\frac{1}{6}}. \tag{47}$$

If we further take $P_2^{1\text{keV}} \approx 0.6$ as discussed above, then we obtain the predicted parameter values shown in Fig. 5a. We see that P_2 is, indeed, expected to increase under these assumptions, and if we insert this result into Eq. (44) and solve numerically for θ_C, we obtain the behavior shown in Fig. 5b. We observe that the predicted critical angle increases around 1.5 keV for our hypothesized values of P_1 and P_2, consistent with the disappearance of ripples at $65°$ observed in [53] for Ar^+-irradiated Si.

Physical intuition We conclude this section by developing some physical intuition as to why, exactly, the Boundary Amorphization mechanism is unconditionally stabilizing, and why it and a correct model of interfacial geometry must be handled simultaneously. The former follows directly from the nature of the amorphization

boundary condition (11). This condition induces an extra, inward-normal component of the velocity field at the amorphous–crystalline boundary, with the magnitude of this extra velocity determined by the amorphization rate— hence the erosion rate $Y(\theta)$. Because the extra velocity component is directed in the *normal* direction, it has the effect of directing newly amorphized material away from the peaks of the lower interface. Now, although we saw in Sect. 3 that the lower interface is not directly below the upper interface, we also noted in Sect. 4 that ion-induced nanopatterns tend to exhibit "long-wave" behavior. Therefore, the peaks and valleys of the upper and lower interfaces are *nearly* aligned, and so the "extra" flow due to amorphization moves toward the valleys of the upper interface, which is stabilizing.

The mechanism just described is independent of the angle of the ion beam, and hence, unconditionally stabilizing. Nevertheless, the angle-dependent film thickness $h_0(\theta)$ plays a crucial role. For a fixed inward-normal velocity profile along the amorphous–crystalline interface, the stabilization just described is the greatest when the film thickness is least (because the thinner the film, the less room this extra flow component has to dissipate). When the film thickness is taken as a constant with respect to the incidence angle (the "vertical translation" limit), the $\frac{\Omega Y(\theta)}{h_0(\theta)} \left(1 - \frac{\rho_a}{\rho_c}\right)$ term must under-predict stabilization, as the denominator is too large. Similarly, if the film thickness is taken to decay as $\cos(\theta)$ (the "diagonal translation" limit), this same term grows too quickly in θ, developing a singularity at $\theta = 90°$, and dramatically *over-predicting* stabilization in the approach to grazing incidence. Hence a proper treatment of Boundary Amorphization and its contribution to thin-film stability requires a more detailed treatment of angle-dependent film thickness.

6 Conclusions

Here we review the main contributions offered and questions highlighted in this work.

Improved interfacial modeling leads to better predictions As described above, the amorphous–crystalline interface has previously been modeled variously as flat [72, 81], a vertical translation of the free interface [24, 65], or a "diagonal" translation of the free interface [42, 63]. However, as we have previously shown, the choice of an interface relation leads to significant differences in predictions for the critical angle θ_C, complicating the reconciliation of theory and experiment [65]. In response, we have derived an improved description of the lower interface position, informed directly by collision cascade statistics that are obtainable from simulations. This approach produces excellent agreement with experimentally inferred film thicknesses for 1keV $Ar^+ \rightarrow Si$, and predictions of the critical angle in between those of simple "vertical" and "diagonal" interface translations. Most importantly, this more accurate boundary location eliminates a significant source of uncertainty from past models.

At the same time, we have also considered a refinement in the treatment of the amorphous–crystalline interfacial physics, by including the change in density accompanying the crystalline-to-amorphous phase-change. This mechanism produces an additional term in the dispersion relation, which is increasingly stabilizing as the incidence angle θ increases. This term leads to a sudden, sharp increase in the critical angle

above a certain value of the dimensionless parameter P_2. Subject to the hypotheses on the energy dependence of P_2 described above, this coincides quite well with the energetic regime at which patterns appear to be strongly suppressed for $Ar^+ \rightarrow Si$. Finally, we remark that the present model cannot explain the return of patterns at much higher energies [53]; however, the assumptions of the Davis scaling [79] have certainly broken down well before these energies. This naturally provides an avenue for future work.

Need for unified models of viscosity and stress While the modeling improvements described here appear to offer improved predictive capability, they also highlight significant modeling uncertainties in the treatment of key physical constants. Namely, the parametric dependence of the ion-enhanced fluidity η^{-1} and ion-induced stress A_D remain largely unknown, frustrating efforts to unify predictions across target species, ion species, ion energy (especially at much higher energies, as noted immediately above), and ion flux.

Although the idea of an ion-enhanced fluidity dates to at least [21, 22], there remains no experimentally verified first-principles explanation for the origin of this effect. Many works needing estimates of the fluidity extrapolate from a single molecular dynamics study [50, 51], while a few others draw inferences from a limited number of experiments on irradiated cantilevers [39, 41]. Within the ion-induced nanopatterning literature, we are aware of only one model attempting to make predictions based on underlying physics [40].

Similarly, the idea of an ion-induced stress has been used within the literature since at least [36]. At high ion energies (the "electronic stopping" regime [16, 48, 78]), a plausible physical model of the effect exists [37, 56, 70], but at low energies (the "nuclear stopping" regime [16, 48, 78]), its use is essentially phenomenological [5, 24]. Here, we have used the energy dependence proposed by Davis [79], an analogy first used within the ion-induced nanopatterning literature by [42]. However, without a direct physical model, the conditions under which this analogy holds remain speculative.

These two uncertainties are intimately related, because a fluid's viscosity dictates its ability to relax bulk stresses induced by the ion beam. This in turn affects the steady stress predicted to arise due to Anisotropic Plastic Flow. As we saw above, this steady stress takes the form $|\mathbf{T}_0| = 6 f A_D \eta$—the *product* of the two unknown quantities. In certain circumstances, an empirical measurement of this product is sufficient to compare with theory [24]. However, a full understanding of ion-induced pattern formation requires independent estimates of these distinct quantities.

Declarations

Conflict of interest The authors have no Conflict of interest to declare that is relevant to the content of this article.

Appendix A: Details of linear stability analysis

A.1 Expansion: small perturbative wavenumber *k*

Here, we show the details of the long-wave expansion. As described in the main text, we expand as

$$\sigma = 0 + k\sigma_1 + k^2\sigma_2 + \mathcal{O}(k^3), \tag{A.1}$$

and we obtain the following systems at each order in k.

At $\mathcal{O}(1)$:

$$
\begin{aligned}
&\rho_{0z}\tilde{w}_{10} + \rho_0\tilde{w}'_{10} + \tilde{\rho}'_{10}w_0 + \tilde{\rho}_{10}w_{0z} = 0, \\
&\tilde{u}''_{10} = 0, \\
&- \tilde{p}'_{10} + 2\eta w''_{10} = 0, \\
&\tilde{\rho}_{10} = \frac{-\rho_a\tilde{\Delta}_{10}}{(1+\Delta_0)^2}, \\
&w_0\tilde{\Delta}'_{10} + \tilde{w}_{10}\Delta_{0z} = 0.
\end{aligned}
\tag{A.2}
$$

At $z = 0$,

$$
\begin{aligned}
&\Delta_{0z}g_1 + \tilde{\Delta}_{10} = 0, \\
&\tilde{u}_{10} + u_{0z}\tilde{g}_1 = 0, \\
&\tilde{w}_{10} + w_{0z}\tilde{g}_1 = 0.
\end{aligned}
\tag{A.3}
$$

At $z = h_0$,

$$
\begin{aligned}
&\tilde{w}_{10} + \tilde{h}_1 w_{0z} + \frac{V\rho^*}{\rho_0^2}(\rho_{0z}\tilde{h}_1 + \tilde{\rho}_{10}) = 0, \\
&\eta\tilde{u}'_{10} = 0, \\
&- \tilde{p}_{10} + 2\eta\tilde{w}'_{10} + T_{0z}^{33} = 0.
\end{aligned}
\tag{A.4}
$$

At $\mathcal{O}(\epsilon k)$:

$$
\begin{aligned}
&\sigma_1\tilde{\rho}_{10} + i\rho_0\tilde{u}_{10} + \rho_{0z}\tilde{w}_{11} + \rho_0\tilde{w}'_{11} + \tilde{\rho}'_{11}w_0 + \tilde{\rho}_{11}w_{0z} = 0, \\
&- i\tilde{p}_{10} + \eta(\tilde{u}''_{11} + i\tilde{w}'_{10}) = 0, \\
&- \tilde{p}'_{11} + \eta(2\tilde{w}''_{11} + i\tilde{u}'_{10}) = 0, \\
&\tilde{\rho}_{11} = \frac{-\rho_a\tilde{\Delta}_{11}}{(1+\Delta_0)^2}, \\
&\sigma_1\tilde{\Delta}_{10} + iu_0\tilde{\Delta}_{10} + w_0\tilde{\Delta}'_{11} + \tilde{w}_{11}\Delta_{0z} = 0.
\end{aligned}
\tag{A.5}
$$

At $z = 0$,

$$\tilde{\Delta}_{11} = 0,$$
$$\tilde{u}_{11} + i\tilde{g}_1(w_0 - V) = 0,$$
$$-i\tilde{g}_1 u_0 + \tilde{w}_{11} = \left(\frac{\rho_a - \rho_c}{\rho_a}\right)\sigma_1\tilde{g}_1. \tag{A.6}$$

At $z = h_0$,

$$\sigma_1\tilde{h}_1 = \tilde{w}_{11} - u_0 i\tilde{h}_1 + \frac{V\rho_c}{\rho_0^2}\tilde{\rho}_{11},$$
$$\eta(\tilde{u}'_{11} + i\tilde{w}_{10}) - i\tilde{h}_1 T_0^{11} = 0, \tag{A.7}$$
$$-\tilde{p}_{11} + 2\eta\tilde{w}'_{11} = 0.$$

At $\mathcal{O}(\epsilon k^2)$:

$$\sigma_1\tilde{\rho}_{11} + \sigma_2\tilde{\rho}_{10} + i\rho_0\tilde{u}_{11} + \rho_{0z}\tilde{w}_{12} + \rho_0\tilde{w}'_{12} + \tilde{\rho}'_{12}w_0 + \tilde{\rho}_{12}w_{0z} = 0,$$
$$-i\tilde{p}_{11} + \eta(-2\tilde{u}_{10} + \tilde{u}''_{12} + i\tilde{w}'_{11}) = 0,$$
$$-\tilde{p}'_{12} + \eta(-\tilde{w}_{10} + 2\tilde{w}''_{12} + i\tilde{u}'_{11}) = 0, \tag{A.8}$$
$$\tilde{\rho}_{12} = \frac{-\rho_a\tilde{\Delta}_{12}}{(1 + \Delta_0)^2},$$
$$\sigma_1\tilde{\Delta}_{11} + \sigma_2\tilde{\Delta}_{10} + iu_0\tilde{\Delta}_{11} + w_0\tilde{\Delta}'_{12} + \tilde{w}_{12}\Delta_{0z} = 0$$

at $z = 0$,

$$\tilde{\Delta}_{12} = 0,$$
$$\tilde{u}_{12} = 0,$$
$$\tilde{w}_{12} = \left(\frac{\rho_a - \rho_c}{\rho_a}\right)\sigma_2\tilde{g}_1, \tag{A.9}$$

and at $z = h_0$,

$$\sigma_2\tilde{h}_1 = \tilde{w}_{12} + \frac{V\rho_c}{\rho_0^2}\tilde{\rho}_{12},$$
$$\eta(\tilde{u}'_{12} + i\tilde{w}_{11}) = 0, \tag{A.10}$$
$$-\tilde{p}_{12} + 2\eta\tilde{w}'_{12} = 0.$$

A.2 Third expansion: small swelling rate fA_I

A third expansion in small swelling rate fA_I is motivated by two observations. First, from previous results [64], it is known that the effect of even large swelling rates is highly self-similar at all wave numbers, and uniformly stabilizing for long waves.

Second, as was seen in [63, 65], the expansion in small swelling rate is conducive to analytical solution; while it may be possible to solve the long-wave equations for arbitrary swelling rate analytically (as in [64]), the Appendix in [65] suggests that the linearized equations are substantially more complicated even in the long-wave limit. Hence we take

$$
\begin{aligned}
\alpha &= \alpha_0 + f A_I \alpha_1 + ..., \\
\rho_0 &= \rho_{00} + f A_I \rho_{01} + ..., \\
&\quad ... \\
\sigma_1 &= \sigma_{10} + f A_I \sigma_{11} + ..., \\
\tilde{\rho}_{10} &= \tilde{\rho}_{100} + f A_I \tilde{\rho}_{111} + ..., \\
&\quad ...
\end{aligned}
\tag{A.11}
$$

In following with [65], we shall only write out explicitly the equations expanded in $f A_I$, as the equations for the leading order terms are obvious from the above (simply by appending a "0" to the subscript of each term). We then obtain the following.

Steady state at $\mathcal{O}(f A_I)$:

$$
\begin{aligned}
&\frac{\partial}{\partial z}(\rho_{00} w_{01} + \rho_{01} w_{00}) = 0, \\
&\eta u_{01zz} = 0, \\
&- p_{01z} + 2\eta w_{01zz} = 0 \\
&\rho_{01} = \frac{-\rho_a \Delta_{01}}{(1 + \Delta_{00})^2}, \\
&w_{00}\Delta_{01z} + w_{01}\Delta_{00z} = 1.
\end{aligned}
\tag{A.12}
$$

At z = 0:

$$
\begin{aligned}
\Delta_{01} &= 0, \\
u_{01} &= 0, \\
w_{01} &= 0.
\end{aligned}
\tag{A.13}
$$

At $z = h_0$,

$$
\begin{aligned}
w_{01} + V \rho_c \frac{\rho_{01}}{\rho_{00}^2} &= 0, \\
u_{01z} &= 0, \\
- p_{01} + 2\eta w_{01z} &= 0.
\end{aligned}
\tag{A.14}
$$

At $\mathcal{O}(\epsilon f A_I)$:

$$\rho_{00z}\tilde{w}_{101} + \rho_{01z}\tilde{w}_{100} + \rho_{00}\tilde{w}_{101z} + \rho_{01}\tilde{w}_{100z} + \tilde{\rho}_{100z}w_{01},$$
$$+ \ \tilde{\rho}_{101z}w_{00} + \tilde{\rho}_{100}w_{01z} + \tilde{\rho}_{101}w_{00z} = 0$$
$$\tilde{u}_{101zz} = 0,$$
$$-\tilde{p}_{101z} + 2\eta\tilde{w}_{101zz} = 0, \qquad\qquad\qquad (A.15)$$
$$w_{00}\tilde{\Delta}_{101z} + w_{01}\tilde{\Delta}_{100z} + \tilde{w}_{100}\Delta_{01z} + \tilde{w}_{101}\Delta_{00z} = 0,$$
$$\tilde{\rho}_{101} = \frac{-\rho_a(\Delta_{00}\tilde{\Delta}_{101} + \tilde{\Delta}_{101} - 2\Delta_{01}\tilde{\Delta}_{100})}{(1 + \Delta_{00})^3}.$$

At z = 0:

$$\Delta_{01z}\tilde{g}_1 + \tilde{\Delta}_{101} = 0,$$
$$\tilde{u}_{101} + u_{01z}g_1 = 0, \qquad\qquad\qquad (A.16)$$
$$\tilde{w}_{101} + w_{01z}g_1 = 0.$$

At z = h_0:

$$\tilde{w}_{101} + \tilde{h}_1 w_{01z} + V\rho_c\frac{(\rho_{00}(\rho_{01z}h_1 + \tilde{\rho}_{101}) - 2\rho_{01}(\rho_{00z}h_1 + \tilde{\rho}_{100}))}{\rho_{00}^3} = 0,$$
$$\tilde{u}'_{101} = 0, \qquad\qquad\qquad (A.17)$$
$$-\tilde{p}_{101} + 2\eta\tilde{w}'_{101} + T_{01z}^{33} = 0.$$

At $\mathcal{O}(\epsilon k f A_I)$:

$$\sigma_{10}\tilde{\rho}_{101} + \sigma_{11}\tilde{\rho}_{100} + i(\rho_{00}\tilde{u}_{101} + \rho_{01}\tilde{u}_{100}) + (\rho_{00z}\tilde{w}_{111} + \rho_{01z}\tilde{w}_{110}),$$
$$+ (\rho_{00}\tilde{w}'_{111} + \rho_{01}\tilde{w}'_{110}) + (\tilde{\rho}'_{110}w_{01} + \tilde{\rho}'_{111}w_{00}) + (\tilde{\rho}_{110}w_{01z} + \tilde{\rho}_{111}\tilde{w}_{00z}) = 0,$$
$$-i\tilde{p}_{101} + \eta(\tilde{u}''_{111} + i\tilde{w}'_{101}) = 0,$$
$$-\tilde{p}'_{111} + \eta(2\tilde{w}''_{111} + i\tilde{u}'_{101}) = 0,$$
$$\sigma_{10}\tilde{\Delta}_{101} + \sigma_{11}\tilde{\Delta}_{100} + i(u_{00}\tilde{\Delta}_{101} + u_{01}\tilde{\Delta}_{100}) + w_{00}\tilde{\Delta}'_{111}, \qquad (A.18)$$
$$+ w_{01}\tilde{\Delta}'_{110} + \tilde{w}_{110}\Delta_{01z} + \tilde{w}_{111}\Delta_{00z} = 0,$$
$$\tilde{\rho}_{111} = \frac{-\rho_a(\Delta_{00}\tilde{\Delta}_{111} + \tilde{\Delta}_{111} - 2\Delta_{01}\tilde{\Delta}_{110})}{(1 + \Delta_{00})^3}.$$

At z = 0:

$$\tilde{\Delta}_{111} = 0,$$
$$\tilde{u}_{111} + i\tilde{g}_1 w_{01} = 0, \qquad\qquad\qquad (A.19)$$
$$-i\tilde{g}_1 u_{01} + \tilde{w}_{111} = \left(\frac{\rho_a - \rho_c}{\rho_a}\right)\sigma_{11}\tilde{g}_1.$$

At $z = h_0$:

$$\sigma_{11}\tilde{h}_1 = \tilde{w}_{111} - u_{01}i\tilde{h}_1 + \frac{V\rho_c(\rho_{00}\tilde{\rho}_{111} - 2\rho_{01}\tilde{\rho}_{110})}{\rho_{00}^3},$$

$$- i\tilde{h}_1 T_{01}^{11} + \eta\{\tilde{u}'_{111} + i\tilde{w}_{101}\} = 0,$$

$$- \tilde{p}_{111} + 2\eta\tilde{w}'_{111} = 0.$$

(A.20)

At $\mathcal{O}(\epsilon k^2 f A_I)$:

$$\sigma_{10}\tilde{\rho}_{111} + \sigma_{11}\tilde{\rho}_{110} + (\sigma_{20}\tilde{\rho}_{101} + \sigma_{21}\tilde{\rho}_{100}) + i(\rho_{00}\tilde{u}_{111} + \rho_{01}\tilde{u}_{110}),$$

$$+ (\rho_{00z}\tilde{w}_{121} + \rho_{01z}\tilde{w}_{120}) + (\rho_{00}\tilde{w}'_{121} + \rho_{01}\tilde{w}'_{120}),$$

$$+ (\tilde{\rho}'_{120}w_{01} + \tilde{\rho}'_{121}w_{00}) + (\tilde{\rho}_{120}w_{01z} + \tilde{\rho}_{121}w_{00z}) = 0,$$

$$- i\tilde{p}_{111} + \eta(-2\tilde{u}_{101} + \tilde{u}''_{121} + i\tilde{w}'_{111}) = 0,$$

$$- \tilde{p}'_{121} + \eta(-\tilde{w}_{101} + 2\tilde{w}''_{121} + i\tilde{u}'_{111}) = 0,$$

$$\sigma_{10}\tilde{\Delta}_{111} + \sigma_{11}\tilde{\Delta}_{110} + \sigma_{20}\tilde{\Delta}_{101} + \sigma_{21}\tilde{\Delta}_{100} + i(u_{00}\tilde{\Delta}_{111} + u_{01}\tilde{\Delta}_{110}),$$

$$+ w_{00}\tilde{\Delta}'_{121} + w_{01}\tilde{\Delta}'_{120} + \tilde{w}_{120}\Delta_{01z} + \tilde{w}_{121}\Delta_{00z} = 0,$$

$$\tilde{\rho}_{121} = \frac{-\rho_a(\Delta_{00}\tilde{\Delta}_{121} + \tilde{\Delta}_{121} - 2\Delta_{01}\tilde{\Delta}_{120})}{(1 + \Delta_{00})^3}.$$

(A.21)

At $z = 0$:

$$\tilde{\Delta}_{121} = 0,$$

$$\tilde{u}_{121} = 0,$$

$$\tilde{w}_{121} = \left(\frac{\rho_a - \rho_c}{\rho_a}\right)\sigma_{21}\tilde{g}_1.$$

(A.22)

At $z = h_0$:

$$\sigma_{21}\tilde{h}_1 = \tilde{w}_{121} + V\rho_c\left(\frac{\rho_{00}\tilde{\rho}_{121} - 2\rho_{01}\tilde{\rho}_{120}}{\rho_{00}^3}\right),$$

$$\tilde{u}'_{121} + i\tilde{w}_{111} = 0,$$

$$-\tilde{p}_{121} + 2\eta\tilde{w}'_{121} = 0.$$

(A.23)

A.3 Solution

In the limit of small cross-terms, the same as in [65] and discussed in the main text, we obtain

$$\sigma = 0 + \sigma_{10}(kh_0) + f A_I\sigma_{11}(kh_0) + \sigma_{20}(kh_0)^2 + f A_I\sigma_{21}(kh_0)^2$$

$$+ \mathcal{O}\big((kh_0)^3, (f A_I)^2\big)$$

(A.24)

where

$$\sigma_{10} = \frac{-2fA_{Di}D_{13}\left[1 + \frac{\tilde{g}_1}{\tilde{h}_1}\right]}{\left[1 - \left(1 - \frac{\rho_c}{\rho_a}\right)\frac{\tilde{g}_1}{\tilde{h}_1}\right]}, \tag{A.25}$$

$$\sigma_{11} = 0, \tag{A.26}$$

$$\sigma_{20} = \frac{\left[-2fA_D\left(D_{11} - D_{33}\right) + \frac{\tilde{g}_1}{\tilde{h}_1}\frac{V}{h_0}\left(1 - \frac{\rho_c}{\rho_a}\right)\right]}{\left[1 - \left(1 - \frac{\rho_c}{\rho_a}\right)\frac{\tilde{g}_1}{\tilde{h}_1}\right]} \tag{A.27}$$

and

$$\sigma_{21} = \frac{-\frac{\rho_a}{\rho_c}\left[2\frac{\rho_c}{\rho_a} + \left(\frac{\tilde{g}_1}{\tilde{h}_1}\right)^2\left(1 - \frac{\rho_c}{\rho_a}\right)\left(1 + 2\frac{\rho_c}{\rho_a}\right) - \frac{\tilde{g}_1}{\tilde{h}_1}\left(1 + 2\frac{\rho_c}{\rho_a} - 2\frac{\rho_c}{\rho_a}^2\right)\right]}{2\left[1 - \left(1 - \frac{\rho_c}{\rho_a}\right)\frac{\tilde{g}_1}{\tilde{h}_1}\right]^2}. \tag{A.28}$$

Taking

$$\frac{\tilde{g}_1}{\tilde{h}_1} = \exp\left(-ikx_0(\theta)\right) \tag{A.29}$$

as described in the main text and collecting terms at each order of k recovers our main result, Eq. (44).

Appendix B: Mass-conservation boundary condition

We may express conservation of mass as

$$\frac{\mathrm{d}}{\mathrm{d}t}\int_\Omega \rho(\vec{x}, t)\mathrm{d}V = \int_{\partial\Omega} \rho(\vec{x}, t)\left[v_I - \vec{v}(\vec{x}, t)\cdot\hat{n}\right]\mathrm{d}A$$
$$+ \int_{\partial\Omega} S_1(\vec{x}, t)\mathrm{d}A + \int_\Omega S_2(\vec{x}, t)\mathrm{d}V, \tag{B.30}$$

where $\rho(\vec{x}, t)$ is the scalar density field, Ω is a control volume, V_I is the normal velocity of the interface $\partial\Omega$ whose differential surface element is dA, $\vec{v}$ is the bulk velocity field of the substrate that the interface moves through, and $\hat{n}$ is the normal vector to the differential surface element dA. S_1 represents a surface source and S_2 represents a bulk (volumetric) source. Because we are interested in the conservation of mass at the amorphous–crystalline boundary $z = g$, and we expect no mass-sources either at the surface or in the bulk, we take the sources $S_1, S_2 \to 0$. Letting the control volume Vol$(\Omega) \to 0$, conservation requires

$$\int_{\partial\Omega} \rho(\vec{x}, t)\big[v_I - \vec{v}(\vec{x}, t) \cdot \hat{n}_g\big]dA = 0, \tag{B.31}$$

hence

$$\left(\rho(\vec{x}, t)\big[v_I - \vec{v}(\vec{x}, t) \cdot \hat{n}_g\big]\right)_{\text{amorphous}} = \left(\rho(\vec{x}, t)\big[v_I - \vec{v}(\vec{x}, t) \cdot \hat{n}_g\big]\right)_{\text{crystalline}} \tag{B.32}$$

or

$$\left(\rho_a\big[v_I - \vec{v}_a \cdot \hat{n}_g\big]\right) = \left(\rho_c\big[v_I - \vec{v}_c \cdot \hat{n}_g\big]\right). \tag{B.33}$$

Since the underlying crystalline substrate receives vanishingly little energy compared to the amorphous layer, we anticipate that $|\vec{v}_c| \ll |\vec{v}_a|$, such that $\vec{v}_c \approx \vec{0}$ in comparison. Then rearrangement leads to

$$\vec{v}_a \cdot \hat{n} = \left(1 - \frac{\rho_c}{\rho_a}\right)v_I \tag{B.34}$$

at z = g, or, as a jump relation,

$$[[\rho\vec{v}]] \cdot \hat{n} = [[\rho]]v_{I,g}, \tag{B.35}$$

as in the main text. It is noteworthy that when $[[\rho]] = 0$, such that the density of the crystalline and amorphous phases are assumed to be equal, we immediately restore the more typical no-penetration condition. Equivalently, we point out that the common use of the no-penetration condition throughout the literature on hydrodynamic-type approaches to ion-induced pattern formation literature implicitly takes the crystalline and amorphous phases to have the same density. One of the primary results of the present work is that this irradiation-induced change of phase significantly affects the linear stability of the film.

Next, we convert to the traveling frame via

$$\vec{v} \to \vec{v} - V\hat{k}. \tag{B.36}$$

Then, we have

$$v_{I,g} \to v_{I,g} - V\hat{k} \cdot \hat{n}_g \tag{B.37}$$

due to ongoing erosion. These lead to

$$\rho_a \vec{v}_a \cdot \hat{n}_g = (\rho_a - \rho_c)(v_{I,g} - V\hat{k} \cdot \hat{n}_g) + \rho_a V\hat{k} \cdot \hat{n}_g,$$
$$\vec{v}_a \cdot \hat{n}_g = \left(\frac{\rho_a - \rho_c}{\rho_a}\right)(v_{I,g} - V\hat{k} \cdot \hat{n}_g) + V\hat{k} \cdot \hat{n}_g,$$
$$\vec{v}_a \cdot \hat{n}_g = \left(1 - \frac{\rho_c}{\rho_a}\right)v_{I,g} - \left(1 - \frac{\rho_c}{\rho_a}\right)V\hat{k} \cdot \hat{n}_g + V\hat{k} \cdot \hat{n}_g, \qquad \text{(B.38)}$$
$$\vec{v}_a \cdot \hat{n}_g = \left(1 - \frac{\rho_c}{\rho_a}\right)v_{I,g} + \left(\frac{\rho_c}{\rho_a}\right)V\hat{k} \cdot \hat{n}_g.$$

We now drop the subscript a as it is clear that the only bulk velocity field under consideration is that of the amorphous layer. In principle, we have made the assumption that the motion of the amorphous bulk is much faster than that of the underlying crystalline substrate. It is also clear that when $\rho_a = \rho_c$ (i.e., there is no density drop across the interface), and if we assume the typical no-slip condition $u = 0$ at $z = g$, we recover

$$\vec{v} = V\hat{k}. \qquad \text{(B.39)}$$

This is as was seen in [63]. From

$$\vec{v} \cdot \hat{n}_g = \left(1 - \frac{\rho_c}{\rho_a}\right)v_{I,g} + \left(\frac{\rho_c}{\rho_a}\right)V\hat{k} \cdot \hat{n}_g, \qquad \text{(B.40)}$$

the steady-state equation is easily obtained, and we find the following expansions in Fourier modes.
At $\mathcal{O}(\epsilon k^0)$,

$$\tilde{g}_1 w_{0z} + \tilde{w}_{100} = 0. \qquad \text{(B.41)}$$

At $\mathcal{O}(\epsilon k^1)$,

$$-i\tilde{g}_1 u_0 + \tilde{w}_{110} = \sigma_{10}\left(1 - \frac{\rho_c}{\rho_a}\right)\tilde{g}_1. \qquad \text{(B.42)}$$

At $\mathcal{O}(\epsilon k^2)$,

$$\tilde{w}_{120} = \sigma_{20}\left(1 - \frac{\rho_c}{\rho_a}\right)\tilde{g}_1. \qquad \text{(B.43)}$$

Expansion in $f A_I$ is straightforward. Then we arrive at the boundary conditions in the main text. We note that this condition is more typical of the solidification theory literature, and is featured prominently in Chapter 9 of [66] and elsewhere, while being largely absent from most other resources on continuum mechanics, where phase transitions are seldom of interest.

Appendix C: Coefficients for small-slope expansion of lower interface

From the $|h_x| \ll 1$ expansion in the main text, and, bringing our notation into alignment with Fig. 2, we obtain

$$
z^B(\theta, h_x) = z^T - \left[a\cos(\theta) + 2\left(\sqrt{\alpha^2\cos^2(\theta) + \beta^2\sin^2(\theta)} \sqrt{\frac{\ln(\frac{E_0}{E_A})}{2}} \right) \right] + \mathcal{O}(h_x^2),
$$

(C.44)

and

$$
\begin{aligned}
x^B&(\theta, h_x) \\
&= x^T + a\sin(\theta) + 2\left(\frac{(\alpha^2 - \beta^2)\sin(\theta)\cos(\theta)}{\sqrt{\alpha^2\cos^2(\theta) + \beta^2\sin^2(\theta)}} \sqrt{\frac{\ln(\frac{E_0}{E_A})}{2}} \right) \\
&\quad - h_x\left(a\cos(\theta) + \frac{(\alpha^2 - \beta^2)\left(4(\alpha^2 + \beta^2)\cos(2\theta) + (\alpha^2 - \beta^2)(3 + \cos(4\theta))\right)}{(\alpha^2\cos^2(\theta) + \beta^2\sin^2(\theta))^{3/2}} \right) \\
&\quad + \mathcal{O}(h_x^2).
\end{aligned}
$$

(C.45)

In the above, it is clear that the $\mathcal{O}(h_x)$ term in $z^B(\theta, h_x)$ is identically zero, and the next term in the expansion is nonlinear in h_x; its form is therefore irrelevant to the linear stability analysis of our present interest. The $\mathcal{O}(h_x)$ correction to $x^B(\theta, h_x)$ remains irrelevant as discussed in the main text.

References

1. Navez M, Chaperot D, Sella C (1962) Microscopie electronique - etude de lattaque du verre par bombardement ionique. C R Hebd Seances Acad Sci 254:240
2. Facsko S, Dekorsy T, Koerdt C, Trappe C, Kurz H, Vogt A, Hartnagel H.L (1999) Formation of ordered nanoscale semiconductor dots by ion sputtering. Science 285:1551–1553
3. Chan WL, Chason E (2007) Making waves: Kinetic processes controlling surface evolution during low energy ion sputtering. J Appl Phys 101:121301
4. Muñoz-García J, Vázquez L, Castro M, Gago R, Redondo-Cubero A, Moreno-Barrado A, Cuerno R (2014) Self-organized nanopatterning of silicon surfaces by ion beam sputtering. Mater Sci Eng R 86:1–44
5. Norris SA, Aziz MJ (2019) Ion-induced nanopatterning of silicon: toward a predictive model. Appl Phys Rev 6(1):011311
6. Cuerno R, Kim J-S (2020) A perspective on nanoscale pattern formation at surfaces by ion-beam irradiation. J Appl Phys 128(18):180902
7. Cross MC, Hohenberg PC (1993) Pattern formation outside of equilibrium. Rev Mod Phys 65:851–1123
8. Cross M, Greenside H (2009) Pattern formation and dynamics in nonequilibrium systems. Cambridge University Press, Cambridge
9. Sigmund P (1969) Theory of sputtering. I. Sputtering yield of amorphous and polycrystalline targets. Phys Rev 184:383–416

10. Sigmund P (1973) A mechanism of surface micro-roughening by ion bombardment. J Mater Sci 8:1545–1553
11. Bradley RM, Harper JME (1988) Theory of ripple topography induced by ion bombardment. J Vac Sci Technol 6:2390–2395
12. Carter G, Vishnyakov V (1996) Roughening and ripple instabilities on ion-bombarded Si. Phys Rev B 54:17647–17653
13. Davidovitch BP, Aziz MJ, Brenner MP (2007) On the stabilization of ion sputtered surfaces. Phys Rev B 76:205420
14. Nordlund K (1995) Molecular dynamics simulation of ion ranges in the 1–100 keV energy range. Comput Mater Sci 3:448
15. Ghaly M, Nordlund K, Averback RS (1999) Molecular dynamics investigations of surface damage produced by kiloelectronvolt self-bombardment of solids. Philos Mag A 79:795–820
16. Ziegler JF, Biersack JP, Littmark U (1985) The stopping and range of ions in matter. Pergamon, New York
17. Nietiadi ML, Sandoval L, Urbassek HM, Möller W (2014) Sputtering of Si nanospheres. Phys Rev B 90:045417
18. Kalyanasundaram N, Ghazisaeidi M, Freund JB, Johnson HT (2008) Single impact crater functions for ion bombardment of silicon. Appl Phys Lett 92:131909
19. Norris SA, Samela J, Bukonte L, Backman M, Nordlund DFK, Madi CS, Brenner MP, Aziz MJ (2011) Molecular dynamics of single-particle impacts predicts phase diagrams for large scale pattern formation. Nat Commun 2:276
20. Harrison MP, Bradley RM (2014) Crater function approach to ion-induced nanoscale pattern formation: craters for flat surfaces are insufficient. Phys Rev B 89:245401
21. Rudy AS, Smirnov VK (1999) Hydrodynamic model of wave-ordered structures formed by ion bombardment of solids. Nucl Intrum Methods B 159:52–59
22. Umbach CC, Headrick RL, Chang K-C (2001) Spontaneous nanoscale corrugation of ion-eroded SiO_2: the role of ion-irradiation-enhanced viscous flow. Phys Rev Lett 87:246104
23. Castro M, Cuerno R (2012) Hydrodynamic approach to surface pattern formation by ion beams. Appl Surf Sci 258:4171–4178
24. Norris SA (2012) Stress-induced patterns in ion-irradiated silicon: model based on anisotropic plastic flow. Phys Rev B 86:235405
25. Witvrouw A, Spaepen F (1993) Viscosity and elastic constants of amorphous Si and Ge. J Appl Phys 74:7154
26. Belyakov VS, Titov AI (1996) Stationary amorphous layer formation during 5 kev ar+ bombardment of Ge. Radiat Effects Defects Solids 138:231–241
27. Beardmore KM, Grønbech-Jensen N (1999) Direct simulation of ion-beam-induced stressing and amorphization of silicon. Phys Rev B 60:12610–12616
28. Titov AI, Kucheyev SO (2000) Ion beam induced amorphous-crystalline phase transition in si: quantitative approach. Nucl Inst Methods Phys Res B 168:375–388
29. Titov AI, Azarov AY, Belyakov VS (2003) Kinetics of growth of surface amorphous layers under irradiation in silicon with low-energy light ions. Amorph Vitreous Porous Semicond 37:340–346
30. Titov AI, Belyakov VS, Azarov AY (2003) Formation of surface amorphous layers in semiconductors under low-energy light-ion irradiation: experiment and theory. Nucl Inst Methods Phys Res B 212:169–178
31. Titov AI, Azarov AY, Nikulina LM, Kucheyev SO (2006) Mechanism for the molecular effect in si bombarded with clusters of light atoms. Phys Rev B 73:064111
32. Titov AI, Belyakov VS, Azarov AY (2006) Damage buildup in semiconductors bombarded by low-energy ions. Thin Solid Films 515:118–121
33. Chan WL, Chason E (2008) Stress evolution and defect diffusion in Cu during low energy ion irradiation: experiments and modeling. J Vac Sci Technol A 26:44
34. Orchard SE (1962) On surface levelling in viscous liquids and gels. Appl Sci Res 11A:451
35. Windischmann H (1987) An intrinsic stress scaling law for polycrystalline thin films prepared by ion beam sputtering. J Appl Phys 62:1800
36. Volkert CA (1991) Stress and plastic flow in silicon during amorphization by ion bombardment. J Appl Phys 70:3521
37. van Dillen T, Polman A, Onck PR, van der Giessen E (2005) Anisotropic plastic deformation by viscous flow in ion tracks. Phys Rev B 71:024103

38. Kalyanasundaram N, Moore MC, Freund JB, Johnson HT (2006) Stress evolution due to medium-energy ion bombardment of silicon. Acta Mater 54:483–491
39. Madi CS (2011) Linear stability and instability patterns in ion bombarded silicon surfaces. PhD thesis, Harvard University
40. Ishii Y, Madi C, Aziz MJ, Chason E (2014) Stress evolution in Si during low-energy ion bombardment. J Mater Res 29:2942–2948
41. Perkinson JC (2017) PhD thesis, Harvard University
42. Moreno-Barrado A, Castro M, Gago R, Vázquez L, Muñoz-García J, Redondo-Cubero R, Galiana B, Ballesteros C, Cuerno R (2015) Nonuniversality due to inhomogeneous stress in semiconductor surface nanopatterning by low-energy ion-beam irradiation. Phys Rev B 91:155303
43. Norris SA, Perkinson JC, Mokhtarzadeh M, Anzenberg E, Aziz MJ, Ludwig KF Jr (2017) Distinguishing physical mechanisms using GISAXS experiments and linear theory: the importance of high wavenumbers. Sci Rep 7:1–12
44. Myint P, Ludwig K.F, Wiegart L, Zhang Y, Fluerasu A, Zhang X, Headrick RL (2021) Nanoscale dynamics during self-organized ion beam patterning of si. I. ar$^+$ bombardment. Phys Rev B 103:195423
45. Myint P, Ludwig K.F, Wiegart L, Zhang Y, Fluerasu A, Zhang X, Headrick R.L (2021) Nanoscale dynamics during self-organized ion beam patterning of si. II. kr$^+$ bombardment. Phys Rev B 103:195424
46. Bradley RM (2011) Exact linear dispersion relation for the sigmund model of ion sputtering. Phys Rev B 84:075413
47. Norris SA, Brenner MP, Aziz MJ (2009) From crater functions to partial differential equations: A new approach to ion bombardment induced nonequilibrium pattern formation. J. Phys. Cond. Matt. 21:224017
48. Liedke B (2011) Ion beam processing of surfaces and interfaces: modeling and atomistic simulations. PhD thesis, Helmholtz Zentrum Dresden Rossendorf
49. Perkinson JC, Swenson JM, DeMasi A, Wagenbach C, Ludwig KF Jr, Norris SA, Aziz MJ (2018) Sawtooth structure formation under nonlinear-regime ion bombardment. J Phys: Condens Matter 30:30
50. Vauth S, Mayr SG (2007) Relevance of surface viscous flow, surface diffusion, and ballistic effects in kev ion smoothing of amorphous surfaces. Phys Rev B 75:224107
51. Vauth S, Mayr SG (2008) Ion bombardment induced smoothing of amorphous metallic surfaces: experiments versus computer simulations. Phys Rev B 77:155406
52. Teichmann M, Lorbeer J, Ziberi B, Frost F, Rauschenbach B (2013) Pattern formation on Ge by low energy ion beam erosion. New J Phys 15:103029
53. Hofsäss H, Bobes O, Zhang K (2016) Argon ion beam induced surface pattern formation on Si. J Appl Phys 119:035302
54. van Dillen T, Polman A, Fukarek W, van Blaaderen A (2001) Energy-dependent anisotropic deformation of colloidal silica particles under mev au irradiation. Appl Phys Lett 78:910–912
55. van Dillen T, Polman A, van Kats CM, van Blaaderen A (2003) Ion beam-induced anisotropic plastic deformation at 300 kev. Appl Phys Lett 83:4315–4317
56. van Dillen T, van der Giessen T, Onck PR, Polman A (2006) Size-dependent ion-beam-induced anisotropic plastic deformation at the nanoscale by nonhydrostatic capillary stresses. Phys Rev B 74:132103
57. Otani K, Chen X, Hutchinson JW, Chervinsky JF, Aziz MJ (2006) Three-dimensional morphology evolution of SiO$_2$ patterned films under MeV ion irradiation. J Appl Phys 100:023535
58. Appleton BR, Holland OW, Narayan J III, Williams JS, Short KT, Lawson E (1982) Characterization of damage in ion implanted Ge. Appl Phys Lett 41:711–712
59. Holland OW, Appleton BR, Narayan J (1983) Ion implantation damage and annealing in germanium. J Appl Phys 54:2295–2301
60. Jafri ZH, Jeynes C, Webb RP, Wilson IH (1989) Observation of swelling and sputtering of a silicon target under argon ion irradiation using a double marker technique. Vacuum 39:1119–1121
61. Tamulevicius S, Pozela I, Andrulevicius M (1996) A simple model of radiation swelling in silicon. Mater Sci Eng B 40:141–146
62. Giri PK, Raineri V, Franzo G, Rimini E (2001) Mechanism of swelling in low-energy ion-irradiated silicon. Phys Rev B 65:012110
63. Swenson JM, Norris SA (2018) Swelling as a stabilizing mechanism in irradiated thin films. J Phys: Condens Matter 30(30):304003

64. Evans T, Norris S (2022) Swelling as a stabilizing mechanism in irradiated thin films II: effect of swelling rate. J Phys: Condens Matter 34:325302
65. Evans TP, Norris SA (2023) Swelling as a stabilizing mechanism in irradiated thin films: III. Effect on critical angle in a composite model. J Phys: Condens Matter 35:325302
66. Davis SH (2001) Theory of solidification. Cambridge University Press, Cambridge
67. Evans TP (2023) PhD thesis, Southern Methodist University
68. Klaumünzer S, Li C, Löffler S, Rammensee M, Schumacher G, Neitzert HC (1989) Ion-beam-induced plastic deformation: a universial behavior of amorphous solids. Radiat Eff Defects Solids 108:131–135
69. Trinkaus H, Ryazanov AI (1995) Viscoelastic model for the plastic flow of amorphous solids under energetic ion bombardment. Phys Rev Lett 75:5072–5075
70. Trinkaus H (1998) Dynamics of viscoelastic flow in ion tracks: origin of plastic deformation of amorphous materials. Nucl Inst Methods Phys Res B 146:204–216
71. Chini TK, Okuyama F, Tanemura M, Nordlund K (2003) Structural investigation of keV Ar-ion-induced surface ripples in Si by cross-sectional transmission electron microscopy. Phys Rev B 67:205403
72. Norris SA (2012) Stability analysis of a viscoelastic model for ion-irradiated silicon. Phys Rev B 85:155325
73. Hofsäss H (2014) Surface instability and pattern formation by ion-induced erosion and mass redistribution. Appl Phys A 114:401–422
74. Kumar T, Kumar A, Agarwal DC, Lalla NP, Kanjilal D (2013) Ion beam-generated surface ripples: new insight in the underlying mechanism. Nanoscale Res Lett 8:336
75. Cuerno R, Barabási A-L (1995) Dynamic scaling of ion-sputtered surfaces. Phys Rev Lett 74:4746–4749
76. Madi CS, Anzenberg E, Ludwig KF Jr, Aziz MJ (2011) Mass redistribution causes the structural richness of ion-irradiated surfaces. Phys Rev Lett 106:066101
77. George HB, Tang Y, Chen X, Li J, Hutchinson JW, Golovchenko JA, Aziz MJ (2010) Nanopore fabrication in amorphous Si: viscous flow model and comparison to experiment. J Appl Phys 108:014310
78. Wesch W, Wendler E (eds) (2016) Ion beam modification of solids: ion–solid interaction and radiation damage. Springer, Cham
79. Davis CA (1993) A simple model for the formation of compressive stress in thin films by ion bombardment. Thin Solid Films 226:30
80. Hofsäss H (2015) Model for roughening and ripple instability due to ion-induced mass redistribution [addendum to Hofsäss H (2014) Appl Phys A 114:401. Surface instability and pattern formation by ion-induced erosion and mass redistribution"]. Appl Phys A 119:687–695
81. Muñoz-García J, Cuerno R, Castro M (2019) Stress-driven nonlinear dynamics of ion-induced surface nanopatterns. Phys Rev B 100:205421